NIH Public Access
Author Manuscript
Opt Express. Author manuscript; available in PMC 2010 July 6.

Published in final edited form as:
Opt Express. 2009 August 3; 17(16): 13541–13553.

Signal-to-noise and radiation exposure considerations in conventional and diffraction x-ray microscopy

Xiaojing Huang[1], **Huijie Miao**[1], **Jan Steinbrener**[1], **Johanna Nelson**[1], **David Shapiro**[2], **Andrew Stewart**[1], **Joshua Turner**[1], and **Chris Jacobsen**[1,*]

[1]Department of Physics and Astronomy, Stony Brook University, Stony Brook, NY 11794-3800, USA

[2]Advanced Light Source, Lawrence Berkeley National Laboratory, Berkeley, CA 94720, USA

Abstract

Using a signal-to-noise ratio estimation based on correlations between multiple simulated images, we compare the dose efficiency of two soft x-ray imaging systems: incoherent brightfield imaging using zone plate optics in a transmission x-ray microscope (TXM), and x-ray diffraction microscopy (XDM) where an image is reconstructed from the far-field coherent diffraction pattern. In XDM one must computationally phase weak diffraction signals; in TXM one suffers signal losses due to the finite numerical aperture and efficiency of the optics. In simulations with objects representing isolated cells such as yeast, we find that XDM has the potential for delivering equivalent resolution images using fewer photons. This can be an important advantage for studying radiation-sensitive biological and soft matter specimens.

1. Introduction

X-ray microscopy has unique characteristics of short wavelength and high penetration, and is especially well suited to high resolution imaging of several micrometer thick biological specimens [1,2]. As a result, a number of groups have developed high resolution transmission x-ray microscopes (TXMs) using Fresnel zone plate optics for routine, high resolution imaging of biological specimens in both 2D [3,4,5] and more recently in 3D via tomography [6,7], and commercial lab-based [8] and synchrotron-based [9] systems have begun to appear. These TXM systems complement Fresnel zone plate based scanning transmission x-ray microscopes (STXMs) [10,11,12] by delivering higher throughput for a given source, which is especially important when collecting a tilt series of images for tomography.

In any full-field transmission imaging system, one must collect light scattered by the specimen and use it to obtain a projection image (in 2D) or a volume reconstruction (in 3D). In a TXM operating in brightfield incoherent imaging mode, this is done by using a condenser lens to illuminate the specimen, and an objective lens to collect the scattered light and deliver a phased, magnified, real-space image to a detector. Fresnel zone plates are usually used for the high resolution objective lens, with the image typically recorded on an x-ray sensitive charge-coupled device (CCD) detector.

© 2009 Optical Society of America

Chris.Jacobsen@stonybrook.edu.

OCIS codes: (110.7440) X-ray imaging; (050.1940) Diffraction; (110.3010) Image reconstruction techniques; (110.4280) Noise in imaging systems.

NIH-PA Author Manuscript
NIH-PA Author Manuscript
NIH-PA Author Manuscript

NIH-PA Author Manuscript

NIH-PA Author Manuscript

NIH-PA Author Manuscript

An alternative, lensless scheme was proposed in 1980 by Sayre [13], and demonstrated in 1999 by Miao *et al.* [14]: illuminate an isolated specimen with a coherent wave, collect the far-field diffraction pattern, and obtain a reconstructed image by computationally phasing and then inverting the diffraction pattern (such as by using iterative finite-support phase retrieval methods pioneered by Feinup [15]). X-ray diffraction microscopy (XDM; also called x-ray coherent diffraction imaging or CDI) has the advantage that no optics-imposed losses on either the efficiency, or finite numerical aperture, are imposed upon the experiment. However, in x-ray diffraction microscopy the scattered signal must be phased to obtain an image; since the scattered signal drops off significantly at higher spatial frequencies, one must be able to computationally phase weak scattering signals.

In this work we address the following question through simulations: which approach yields more information on an example biological specimen for a given radiation dose? This is an important consideration for radiation-sensitive specimens such as frozen hydrated cells, since in x-ray microscopy (as in electron microscopy) radiation damage is the ultimate resolution-limiting factor.

To answer this question, we simulate x-ray imaging of two biological-cell-like computed objects consisting of lipid membrane, low concentration protein solute, and protein bars of various diameters and orientations inside the "cells." For diffraction microscopy, we simulate the illumination of the cells by a coherent x-ray beam, calculate the resulting diffraction intensity distributions, add shot noise, and reconstruct the images using an iterative phase retrieval algorithm. For conventional microscopy, we calculate the absorption profiles of the cells, convolve them with the point spread function of a representative soft x-ray zone plate, reduce the image intensities according to the efficiency of the zone plate, and add shot noise to the resulting intensity images. We will discuss results of these comparative simulations and the implications for x-ray microscopy of radiation-sensitive specimens.

2. Specimen illumination, dose, and exposure

Consider a specimen that is illuminated by an average of $\bar{n}$ photons per pixel, with a pixel dimension of Δ (and thus an areal exposure of $\bar{n}/\Delta^2$). If an incident beam is attenuated according to the Lambert-Beer law of $I = I_0 \exp[-\mu z]$, where μ is the linear absorption coefficient, then the fraction of energy absorbed per thickness is given by $-dI/dz = \mu I_0 \exp[-\mu z]$, where z is the distance into which the beam has already penetrated the specimen. We can therefore describe the "skin dose" D at $z = 0$ by

$$D=\frac{\bar{n}E_{\text{photon}}\mu}{\Delta^2\rho}, \tag{1}$$

where ρ is the density of the specimen material and E_{photon} is the photon energy. The skin dose D calculation above assumes no escaped energy, which is usually the case for soft x-ray microscopy because of the short range of secondary electrons produced following x-ray absorption and the very low fluorescence yield of the low-Z elements that make up the main part of the mass of biological specimens. The relative biological effectiveness or RBE factor is considered to be equal to unity as usually the case with x-ray photons. Based on the above, we assume a direct proportionality between photons per pixel $\bar{n}$, areal exposure $\bar{n}/\Delta^2$, and absorbed dose D in what follows.

3. Signal and noise in images

In Sec. 3.1, we consider the expected relationship between photon exposure $\bar{n}$ and the signal-to-noise ratio SNR for detecting an object of a given contrast given signal-dependent noise.

NIH-PA Author Manuscript

NIH-PA Author Manuscript

NIH-PA Author Manuscript

This provides a basis for the expectation that SNR should scale with $\bar{n}$. In Sec. 3.2, we consider the problem of estimating the signal-to-noise ratio SNR for imaging of an object based on image correlations in the presence of signal-dependent noise. This provides a method which is used in subsequent SNR calculations based on simulated images.

3.1. Signal-to-noise ratio, and detection of objects

We wish to consider the signal-to-noise ratio for the detection of an object with a specified contrast. We follow here the treatments of Glaeser [16] and Sayre *et al.* [17]. Our goal is to distinguish measurements (such as image pixels) in the case that a unit-incident-flux measurement would lead to a measured intensity of I. To detect an object, assume that the signal is given by the difference between an intensity with a feature present I_f, and the background intensity I_b; that is, the average signal is $\bar{n}|I_f - I_b|$ when each measurement is made with $\bar{n}$ incident photons. In the Gaussian approximation to the Poisson distribution for event counting, the noise can be expressed as the square root variance of each measurement $\sqrt{\bar{n}I}$, and if the noise is uncorrelated from measurement to measurement (which is the case for photon noise) the total noise will be given by the root mean square sum. As a result, the expected signal-to-noise ratio (SNR) is

$$\mathrm{SNR}=\frac{\mathrm{Signal}}{\mathrm{Noise}}=\frac{\bar{n}\left|I_f-I_b\right|}{\sqrt{\left(\sqrt{\bar{n}I_f}\right)^2+\left(\sqrt{\bar{n}I_b}\right)^2}}=\sqrt{\bar{n}}\frac{\left|I_f-I_b\right|}{\sqrt{I_f+I_b}}=\sqrt{\bar{n}}\Theta, \tag{2}$$

where Θ of

$$\Theta=\frac{\left|I_f-I_b\right|}{\sqrt{I_f+I_b}} \tag{3}$$

is a contrast parameter [17] which differs slightly from the usual definition of contrast C as

$$C=\frac{\left|I_f-I_b\right|}{\sqrt{I_f+I_b}}. \tag{4}$$

Based on Eq. (2), a log-log plot of SNR versus incident photon number $\bar{n}$ should follow a straight line with a slope of 1/2 and an ordinate intercept of $\log_{10}\Theta$:

$$\log_{10}\mathrm{SNR}=\log_{10}\left(\sqrt{\bar{n}}\Theta\right)=\frac{1}{2}\log_{10}\bar{n}+\log_{10}\Theta. \tag{5}$$

3.2. Estimation of the signal-to-noise ratio from image correlations

The easiest way to measure signal-to-noise ratio is to compare measured images of an object against the known object itself. While this approach can be used in simulations, we wish to employ a method that can be used in experiments where the object is not known except through images that have been obtained. An intuitive approach is to calculate the cross correlation coefficient of two independent images of the same object, so as to compare features that are reproduced against those that fluctuate. We summarize here an approach described by Bershad and Rockmore [18] and first used in electron microscopy by Frank and Al-Ali [19]. We extend

NIH-PA Author Manuscript

NIH-PA Author Manuscript

NIH-PA Author Manuscript

this method to signal-dependent noise cases, and cases where the signal is not required to have a mean of zero (such as in intensity rather than amplitude measurements).

Let us consider two separate 2D intensity measurements I_1 and I_2 of the same signal array S with stochastic noise arrays N_1 and N_2, or

$$I_1 = S + N_1 \quad \text{and } I_2 = S + N_2, \tag{6}$$

where the mean value of S over all 2D pixels is $\langle S \rangle$, and N_1 and N_2 come from the same source obeying the same Gaussian distribution with zero mean value ($\langle N_1 \rangle = \langle N_2 \rangle = 0$). As a result, $\langle I_1 \rangle = \langle I_2 \rangle = \langle S \rangle$.

The imaging of a 2D object depends both on how the signal changes across the object due to illumination and the object's intrinsic contrast, and on fluctuations due to noise. We characterize both of these by defining the total signal and noise for the entire 2D image with their variances:

$$\text{Signal}^2 = \langle (S - \langle S \rangle)(S - \langle S \rangle)^* \rangle = \langle S^2 \rangle - \langle S \rangle^2, \tag{7}$$

$$\text{Noise}^2 = \langle (N_{1,2} - \langle N_{1,2} \rangle)(N_{1,2} - \langle N_{1,2} \rangle)^* \rangle = \langle N_{1,2}^2 \rangle, \tag{8}$$

where $\langle N_{1,2} \rangle = 0$ has been used in the final equality of Eq. (8). Again, the average is done over all pixel indices of one 2D image, which differs from a variance calculation for a particular pixel in a set of separately measured images. The variances of images I_1 and I_2 can be calculated as

$$\sigma_{1,2}^2 = \langle (I_{1,2} - \langle I_{1,2} \rangle)(I_{1,2} - \langle I_{1,2} \rangle)^* \rangle = \langle S^2 \rangle + \langle N_{1,2}^2 \rangle - \langle S \rangle^2, \tag{9}$$

where we used the fact that the cross terms $\langle SN_{1,2} \rangle$ are in practice negligible compared to $\langle S^2 \rangle$. This would be expected for low contrast objects, but in practice it also applies to cases with high contrast objects; in simulations, we find that $\langle SN_{1,2} \rangle$ are several orders of magnitude lower than $\langle S^2 \rangle$ even with full contrast objects. As a result, we are able to drop the terms $\langle SN_{1,2} \rangle$ that would otherwise appear in Eq. (9). Since N_1 and N_2 obey the same Gaussian distribution, they have identical variances ($\langle N_1^2 \rangle = \langle N_2^2 \rangle$). So, we can denote $\sigma_1 = \sigma_2 = \sigma$. The covariance between I_1 and I_2 can be derived following analogous steps:

$$r\sigma_1\sigma_2 = r\sigma^2 = \langle (I_1 - \langle I_1 \rangle)(I_2 - \langle I_2 \rangle)^* \rangle = \langle S^2 \rangle - \langle S \rangle^2, \tag{10}$$

where r is the correlation coefficient. It can be calculated as

$$r = \frac{\langle (I_1 - \langle I_1 \rangle)(I_2 - \langle I_2 \rangle)^* \rangle}{\sqrt{\langle (I_1 - \langle I_1 \rangle)^2 \rangle \langle (I_2 - \langle I_2 \rangle)^2 \rangle}}. \tag{11}$$

Combining Eqs. (7) and (8) with Eq. (9), we have

NIH-PA Author Manuscript

NIH-PA Author Manuscript

NIH-PA Author Manuscript

$$\sigma^2=(\langle S^2\rangle - \langle S\rangle^2)+\langle N_{1,2}^2\rangle = \text{Signal}^2+\text{Noise}^2. \tag{12}$$

From Eqs. (7) and (10), we have

$$r\sigma^2=\langle S^2\rangle - \langle S\rangle^2=\text{Signal}^2. \tag{13}$$

From Eqs. (12) and (13), we see that the signal-to-noise ratio can be calculated from the correlation coefficient r as

$$\text{SNR}=\sqrt{\frac{\text{Signal}^2}{\text{Noise}^2}}=\sqrt{\frac{r}{1-r}}, \tag{14}$$

which is the square root of the expression $\alpha = r/(1 - r)$ used by Frank and Al-Ali [19].

To confirm that Eq. (14) provides a good measure of the SNR from multiple noisy images of identical objects, we used simulations to explore its scaling with photon number. As an "object" we used the well-known "Lena" image with transparency I normalized between 0 and 1. For each calculational run we multiplied the image by a value of $\bar{n}$, and then added to each pixel p a pseudo-random noise value based on a positive-integer-truncated Gaussian approximation of the true Poisson distribution for each pixel's value of $\bar{n}I_p$. By repeating this process, we obtained two images of an identical object but with different signal-dependent noise added, allowing us to measure the image SNR using the cross-correlation result of Eqs. (11) and (14). Figure 1(a) shows the resulting images with noise corresponding to the indicated number $\bar{n}$ of incident photons per pixel. Figure 1(b) shows that a log-log plot of the calculated SNR values as a function of $\bar{n}$ has a slope of 1/2 as expected from Eq. (5), reflecting the $\sqrt{\bar{n}}$ dependence of SNR on incident exposure expected from Eq. (2). Finally, we also show in Fig. 1(b) the signal-to-noise ratio calculated by comparison of the original, noise-free image with a noise-included version at each photon exposure $\bar{n}$ using Eqs. (7) and (8). The result shows that these SNR values are identical to those calculated from the cross-correlation method. However, in subsequent calculations we use the two-noisy-image correlation method of Eqs. (11) and (14) because it is applicable to a broader range of cases including experiments where the noise-free object is not known.

4. Simulations with defined "cells"

Having established the image correlation method of Eqs. (11) and (14) for estimating SNR from image pairs, we now turn to simulations of the two experimental approaches to be compared (Fig. 4): lens-based imaging (incoherent brightfield imaging in a TXM), and lensless imaging (x-ray diffraction microscopy or XDM). We discuss the "cells" to be "imaged" in Sec. 4.1, the TXM imaging process in Sec. 4.2, and the XDM imaging process in Sec. 4.3.

4.1. Defined "cells" A and B

We generated two different types of biological-cell-like defined objects for our simulations, which we will call cell A and cell B (see Fig. 2). In both cases we assumed an x-ray energy of 520 eV (within the "water window" [17,20] between the carbon and oxygen K absorption edges), and values of the refractive indices calculated according to the tabulation of Henke *et al.* [21] using an assumed stoichiometric composition of $H_{48.6}C_{32.9}N_{8.9}O_{8.9}S_{0.3}$ and density

NIH-PA Author Manuscript

NIH-PA Author Manuscript

NIH-PA Author Manuscript

of ρ = 1.35 g/cm^3 for protein, and $H_{62.5}C_{31.5}O_{6.3}$ with ρ = 1.0 for lipid [22]. The two objects were defined as follows:

Cell A: The first defined object is modeled as a 2D continuous region with irregular boundary and random protein thicknesses over a range of 0 to 500 nm inside (Fig. 2(a)). The entire image is a 256 × 256 pixel array with a pixel size of 15 nm.

Cell B: The second defined object is embedded in the center of a 400 × 400 × 400 pixel ice cube, also with a pixel size of 15 nm. The cell-like object has a diameter of 200 pixels, or 3 microns, with a 3 pixel or 45 nm thick lipid membrane as boundary. Inside the object, several 225 nm diameter protein rods were placed (1.8 μm long for the vertical bars, and 1.35 μm long for the horizontal bars), along with some protein ellipsoids (the larger ones are 0.9 × 0.45 μm, and the smaller ones are 0.68 × 0.45 μm in size). A "bud" with a diameter of 1.2 μm was added to the top right shoulder of this fake cell, both in order to break the rotational symmetry for eliminating potential problems with enantiomorphs in XDM, and to approximate the appearance of a budding yeast cell. This object was then assumed to be illuminated by a plane wave, and a multislice propagation process [23,24] was used to generate an exit wave (400 × 400 pixels across) leaving the cube.

In the case of cell A, we have a defined object with broad spatial frequency content due to the random thickness variations inside. In the case of cell B, we have an object with readily recognized structures. The two defined objects are shown in real space in Fig. 2, and in Fourier space in Fig. 3. To compare zone plate imaging with diffraction microscopy, we simulated both imaging techniques on these two different defined objects.

4.2. Zone plate imaging process

X-ray microscopes using synchrotron radiation and Fresnel zone plates for full-field imaging have been in existence for some time [3], and are finding considerable success for 25–40 nm resolution imaging applications, tomographic imaging of frozen hydrated cells [6,7,25], with commercial laboratory source versions now becoming available [8]. We model here a representative microscope with a Fresnel zone plate with 30 nm outermost zone width and 10% diffraction efficiency [26], used in incoherent brightfield mode with a 100% efficient detector. In this case the recorded image intensity is a convolution of the intensity transmitted through the object with the intensity point spread function of the imaging system, or

$$\text{image} = \text{object} * \text{intensity\_psf}. \tag{15}$$

Using the convolution theorem of Fourier transforms $\mathcal{F}\{\}$, the image can be represented as

$$\text{image} = \mathcal{F}^{-1}\{\mathcal{F}\{\text{object}\} \cdot \mathcal{F}\{\text{intensity\_psf}\}\} = \mathcal{F}^{-1}\{\mathcal{F}\{\text{object}\} \cdot \text{MTF}\}, \tag{16}$$

where we used the fact that the modulation transfer function or MTF is the Fourier transform of the intensity point spread function. The MTF can be calculated[27] as

$$\text{MTF} = \begin{cases} \frac{2}{\pi}\left[\cos^{-1}\left(\frac{f}{f_0}\right) - \frac{f}{f_0}\sqrt{1-\left(\frac{f}{f_0}\right)^2}\right] & f \le f_0 \\ 0 & f > f_0, \end{cases} \tag{17}$$

where f represents spatial frequency, and f_0 is the spatial frequency cutoff. For a zone plate with outermost zone width of dr_N (set to be 30 nm in simulation), the cutoff of the incoherent MTF is at a spatial frequency of $f_0 = 1/dr_N$. The integral of Eq. (17) has a numerical value of

NIH-PA Author Manuscript

NIH-PA Author Manuscript

NIH-PA Author Manuscript

0.2 compared to the integral of an MTF of 1 for all frequencies up to the cutoff at f_0. The resulting image intensity was then multiplied by 0.1 to account for a typical zone plate focusing efficiency of 10% (while theoretical efficiencies can approach 20%, 10% is representative of the best experimental measurements). Finally, the resulting image was multiplied by an exposure of $\bar{n}$ photons per pixel, and simulated photon noise was added using the positive-integer-truncated Gaussian approach to yield a final image. An image pixel size of 15 nm was used in these simulations.

4.3. Reconstruction from diffraction pattern

In x-ray diffraction microscopy, the image is reconstructed from the far-field diffraction intensity of a coherently illuminated object which is assumed to be within a finite support (area of non-zero optical interaction). To simulate the imaging process, the complex exit waves leaving the defined objects were multiplied by $\sqrt{\bar{n}}$ to account for an exposure of $\bar{n}$ photons per pixel, after which they were Fourier transformed to yield the far-field diffraction amplitudes. These diffraction amplitudes were then squared to yield the diffraction intensities, and simulated photon noise was added to produce the simulated data recordings. The diffraction patterns were assumed to be recorded in the far field, with proper Shannon sampling between the real-space object array and the Fourier plane detector array (that is, 256^2 detector pixels for Cell A, and 400^2 detector pixels for Cell B). As with the TXM case, a real space image pixel size of 15 nm was used in these simulations. To reconstruct the image, we took the square root of the noisy diffraction intensity to revert to Fourier amplitude, and then reconstructed the image using the difference map algorithm developed by Elser [28] with $\beta = 1.15$.

5. Simulation results

5.1. Image simulation and SNR calculation

We carried out simulation runs for each of the two defined objects (cell A and cell B), using both TXM and XDM, and using incident photon per pixel values of $\bar{n} = \{1,2,5\} \times 10^{\{1,2,3,4,5\}}$ and 1×10^6 (that is, exposures of 1×10^1, 2×10^1, …, 1×10^6). Figure 5 shows some examples of simulated zone plate and reconstructed diffraction images. For each incident photon number $\bar{n}$, we calculated 10 TXM images and 10 XDM images, each with separately simulated signal-dependent photon noise in the intensity recording. From each set of 10 images, one can form 45 different two-image pairs for calculating the SNR using the method of Eqs. (11) and (14) over the region where the object is located (that is, inside the object's support for both the XDM and TXM cases). The final SNR value was calculated from the average of these 45 measurements.

Figure 6 shows plots of $\log_{10}(\text{SNR})$ versus $\log_{10}(\bar{n})$ for the set of image simulations of both defined objects. As can be seen, in each case the slope of the fitted line is near 1/2, as expected from Eq. (5); in other words, the signal-to-noise ratio is proportional to $\sqrt{\bar{n}}$ as expected from Eq. (2). An important difference is that x-ray diffraction microscopy gives a higher SNR for a given photon exposure $\bar{n}$ in these simulations. For zone plates of 10% efficiency and an incoherent brightfield MTF integral about 0.2 as described in Sec. 4.2, one might expect a factor of $1/(0.1 \times 0.2) = 50$ in signal loss, or a factor of $\sqrt{50} \simeq 7$ in the signal-to-noise ratio decrease for TXM. The fitted lines of Fig. 6 are indeed higher for x-ray diffraction microscopy versus transmission x-ray microscopy, with an improvement of XDM/TXM of 7.2 ± 1.6 for cell A, and 6.3 ± 2.1 for cell B. This means that the iterative reconstruction algorithm used in x-ray diffraction microscopy is able to phase even weak diffracted signals with significant signal-dependent photon noise present. We also note an early observation by Fienup [15] who found that finite support phase retrieval algorithms appeared to be quite robust in the presence of signal-independent noise added to the Fourier magnitudes.

NIH-PA Author Manuscript

NIH-PA Author Manuscript

NIH-PA Author Manuscript

As noted in Fig. 6, the $\log_{10}$(SNR) versus $\log_{10}(\bar{n})$ dependence of cell B shows some oscillations about the linear trend. This oscillation corresponds to successive Airy rings in the diffraction pattern of the overall spherical shape of cell B, as shown in Fig. 3. In the dark bands between Airy rings corresponding to the far-field diffraction pattern of a disk, the signal is lower than the ring-free trend would suggest that the addition of more photons is less helpful until the next Airy ring begins to be filled in. A different effect can be seen in the $\log_{10}$(SNR) versus $\log_{10}(\bar{n})$ curve for cell A: as shown in Fig. 3, the normalized power spectrum for cell A "levels off" at a constant value of about 10^{-2} at spatial frequencies f above about 10 μm^{-1}. This suggests that when the incident photon number $\bar{n}$ is larger than 100, all the diffraction intensity pixel values approach 1 so that all spatial frequencies above 10 μm^{-1} have measurable, single-photon or larger intensities, and start to contribute to increase reconstruction quality. This may explain the slight flattening of the $\log_{10}$(SNR) versus $\log_{10}(\bar{n})$ curve at the lowest photon exposures for cell A in x-ray diffraction microscopy (XDM).

5.2. Resolution estimation

As shown in Fig. 3, the azimuthally-averaged diffracted signal $P(f)$ in our defined objects declines in a power law relationship of $\log_{10} P(f) = m\log_{10} f + b$ or

$$P(f)=10^b f^m \tag{18}$$

with $m = -3.3$ (azimuthal averaging smooths out the sharp variations due to individual speckles to reveal an overall scattering trend). Theoretical estimates for signal decline in x-ray diffraction microscopy have ranged from $m = -4$ [29], to $m = -3$, -4, and -6 for various specimen models [30]. In small angle x-ray scattering, Porod's law suggests that the diffraction signal should decline with spatial frequency as f^m with $m = -4$, while measured power spectra tend to have positive deviations from this dependence (*i.e.*, values of m of -3 to -4).

As the diffracted signal for a particular length scale declines, the available number of photons for reconstructing structure at that length scale decreases; the signal-to-noise ratio then worsens as a result (as illustrated in Fig. 1). Since images become unrecognizable when a minimum signal-to-noise ratio is not satisfied [31], this suggests a direct relationship between achievable resolution $\Delta_{\min}$ and some minimum signal level $S_{\min}$. Since the signal scales with incident photons per pixel $\bar{n}$ yet declines with spatial frequency f in the Fourier domain, we will assume that the minimum reconstructable signal level is reached at a cutoff spatial frequency f_c, or

$$S_{\min}=\bar{n}P(f_c). \tag{19}$$

Associating the minimum object size $\Delta_{\min}$ with the half-period of a grating at the maximum resolvable spatial frequency f_c, we obtain

$$f_c=\frac{1}{2\Delta_{\min}}. \tag{20}$$

Inserting the diffracted signal trend of Eq. (18) evaluated at frequency f_c into Eq. (19) and then employing Eq. (20) leads to

$$S_{\min}=\bar{n}10^b(2\Delta_{\min})^{-m_r}, \tag{21}$$

NIH-PA Author Manuscript

NIH-PA Author Manuscript

NIH-PA Author Manuscript

where we have used m_r to denote the power law dependence in reconstructed images even though we expect it to be the same as the specimen diffracted power scaling m of Eq. (18). The result of Eq. (21) can then be rearranged to give

$$\log_{10}\bar{n}=m_r\log_{10}(\Delta_{\min})+m_r\log_{10}2+\log_{10}S_{\min}-b, \tag{22}$$

where we have chosen to place $\Delta_{\min}$ on the abscissa and $\bar{n}$ on the ordinate for comparison with the dose-versus-resolution plots estimated by Howells *et al.* [29] and Shen *et al.* [30].

The above arguments suggest that the required dose (proportional to exposure $\bar{n}$) for achieving a desired resolution $\Delta_{\min}$ should have the same log-log slope m_r as the scaling m in object's diffracted signal (because of the use of Eq. (19) in deriving Eq. (22)).We therefore explored the scaling parameter m_r in our simulations of imaging defined cell B using x-ray diffraction microscopy. The spatial frequency dependent ratio $\langle I_{\text{recon}}(f)\rangle / \langle I_{\text{data}}(f)\rangle$ provides a good measure of the resolution in diffraction microscopy reconstructions [24,32] (similar to a phase retrieval transfer function [33]), and in our simulations we used a value of 0.7 for this ratio as a way to identify the cutoff spatial frequency f_c and thus the resolution $\Delta_{\min} = 1/(2\,f_c)$. The resulting data of signal level $\bar{n}$ required to achieve a given resolution $\Delta_{\min}$ are shown in Fig. 7; a linear fit of the data gives a value of $m_r = -3.2 \pm 0.2$. Since defined cell B has a signal that scales like $P(f) \propto f^m$ with $m = -3.30 \pm 0.03$ as shown in Fig. 3, these simulation results are consistent with the expected result: the scattering strength of the specimen determines the dose versus resolution trend for imaging the specimen. The same conclusion is also obtained from cell A.

While Fig. 7 shows a good overall agreement between the dose-versus-resolution slope m_r and the scattering-versus-spatial-frequency slope m, there are "local" departures from this "global" trend. That is, the power law fit of Fig. 7 is done over a very large, 10^5:1 dynamic range in incident photons per pixel $\bar{n}$; this is the "global" trend. If one were instead to carry out the fit over a smaller exposure dynamic range, a different, "local" power law dependance might be observed. Given that the Airy ring characteristics of our defined object B produce departures from a simple power law relationship as seen in Fig. 3 (due to concentration of extra diffraction signal into certain spatial frequency ranges), we expect that both computer simulations and experimental observations can have somewhat different dose-versus-resolution slopes m_r over particular exposure ranges.

6. Conclusions

The goal of this work was to better understand the tradeoffs between two different x-ray microscopy methods for high resolution imaging of dose-sensitive specimens. Although in these simulations we had perfect knowledge of the objects that were "imaged," we chose to adopt a cross-correlation method for quantitative comparisons that is better suited to experimental work with unknown objects. Following the work of Bershad and Rockmore [18], we modified the signal-to-noise measure of Frank and Al-Ali [19] with the result that our measure gives the expected scaling with incident photon number $\bar{n}$. We then used this method to compare incoherent brightfield imaging in a transmission x-ray microscope with a zone plate objective lens of specified efficiency versus x-ray diffraction microscopy using an iterative phase retrieval algorithm for image reconstruction. In these simulations, x-ray diffraction microscopy gave a higher signal-to-noise ratio for equivalent dose, with a gain consistent with the losses imposed by the modulation transfer function and overall efficiency of the zone plate objective.

NIH-PA Author Manuscript

NIH-PA Author Manuscript

NIH-PA Author Manuscript

Of course these simulations are idealized; real imaging experiments involve a number of factors not accounted for here. One of them is that transmission x-ray microscopy has the significant advantage of providing images immediately, unlike x-ray diffraction microscopy where one must use sophisticated image reconstruction algorithms, and specimens that satisfy a finite-support constraint (though we note that ptychography can remove that latter limitation [34]). A limitation of transmission x-ray microscopy as well as its scanning "cousin" is that the resolution-determining outermost zones on zone plates usually have a lower diffraction efficiency than the coarser, inner zones. In x-ray diffraction microscopy, complications include undesired scattering from nearby high-contrast objects such as specimen support grid bars, and the detrimental effects of partial coherence which can contribute noise to reconstructed images [35]. Nevertheless, the simulations shown here illustrate how x-ray diffraction microscopy has the potential to deliver images with higher resolution when studying dose-sensitive specimens.

Acknowledgments

We wish to thank the Division of Materials Sciences and Engineering, Office of Basic Energy Sciences, at the Department of Energy for support of x-ray diffraction microscopy methods and instrumentation development under contract DE-FG02-07ER46128. We also wish to thank the National Institute for General Medical Services at the National Institutes for Health for support of the application of this method to biological imaging under contract 5R21EB6134. Finally, we thank Janos Kirz, Stefano Marchesini, and David Sayre for many helpful discussions in connection with this paper.

References and links

1. Sayre D, Kirz J, Feder R, Kim DM, Spiller E. Potential operating region for ultrasoft x-ray microscopy of biological specimens. Science 1977;196:1339–1340. [PubMed: 867033]
2. Kirz J, Jacobsen C, Howells M. Soft x-ray microscopes and their biological applications. Quart. Rev. Biophys 1995;28:33–130.
3. Niemann B, Rudolph D, Schmahl G. X-ray microscopy with synchrotron radiation. Appl. Opt 1976;15:1883–1884. [PubMed: 20165284]
4. Schmahl G, Rudolph D, Niemann B, Christ O. Zone-plate X-ray microscopy. Quart. Rev. Biophys 1980;13:297–315.
5. Schneider G. Cryo x-ray microscopy with high spatial resolution in amplitude and phase contrast. Ultramicroscopy 1998;75:85–104. [PubMed: 9836467]
6. Weiβ D, Schneider G, Niemann B, Guttmann P, Rudolph D, Schmahl G. Computed tomography of cryogenic biological specimens based on x-ray microscopic images. Ultramicroscopy 2000;84:185–197. [PubMed: 10945329]
7. Larabell C, Le Gros M. X-ray tomography generates 3-D reconstructions of the yeast, *Saccharomyces cerevisiae*, at 60-nm resolution. Molecular Biology of the Cell 2004;15:957–962. [PubMed: 14699066]
8. Tkachuk A, Duewer F, Cui H, Feser M, Wang S, Yun W. X-ray computed tomography in Zernike phase contrast mode at 8 keV with 50-nm resolution using Cu rotating anode x-ray source. Zeitschrift Kristallographie 2007;222:650–655.
9. Yin G-C, Tang M-T, Song Y-F, Chen F-R, Liang K, Duewer F, Yun W, Ko C-H, Shieh H-P. Energy-tunable transmission x-ray microscope for differential contrast imaging with near 60 nm resolution tomography. Appl. Phys. Lett 2006;88 241, 115.
10. Rarback, H.; Kenney, JM.; Kirz, J.; Howells, MR.; Chang, P.; Coane, PJ.; Feder, R.; Houzego, PJ.; Kern, DP.; Sayre, D. Recent results from the Stony Brook scanning microscope. In: Schmahl, G.; Rudolph, D., editors. X-ray Microscopy, vol. 43 of Springer Series in Optical Sciences. Berlin: Springer-Verlag; 1984. p. 203-215.
11. Maser J, Osanna A, Wang Y, Jacobsen C, Kirz J, Spector S, Winn B, Tennant D. Soft x-ray microscopy with a cryo STXM: I. Instrumentation, imaging, and spectroscopy. J. Microsc 2000;197:68–79. [PubMed: 10620150]
12. Kilcoyne A, Tyliszczak T, Steele W, Fakra S, Hitchcock P, Franck K, Anderson E, Harteneck B, Rightor E, Mitchell G, Hitchcock A, Yang L, Warwick T, Ade H. Interferometer-controlled scanning

NIH-PA Author Manuscript

NIH-PA Author Manuscript

NIH-PA Author Manuscript

transmission X-ray microscopes at the Advanced Light Source. J. Synchrotron. Radiat 2003;10:125–136. [PubMed: 12606790]

13. Sayre, D. Prospects for long-wavelength X-ray microscopy and diffraction. In: Schlenker, M., editor. Imaging Processes and Coherence in Physics. Berlin: Springer-Verlag; 1980. p. 229-235.
14. Miao J, Charalambous P, Kirz J, Sayre D. An extension of the methods of x-ray crystallography to allow imaging of micron-size non-crystalline specimens. Nature 1999;400:342–344.
15. Fienup J. Reconstruction of an object from the modulus of its Fourier transform. Opt. Lett 1978;3:27–29. [PubMed: 19684685]
16. Glaeser, RM. Radiation Damage and Biological Electron Microscopy. In: Siegel, BM.; Beaman, DR., editors. Physical aspects of electron microscopy and microbeam analysis. New York: Wiley; 1975. p. 205-227.
17. Sayre D, Kirz J, Feder R, Kim DM, Spiller E. Transmission Microscopy of Unmodified Biological Materials: Comparative Radiation Dosages with Electrons and Ultrasoft X-ray Photons. Ultramicroscopy 1977;2:337–341. [PubMed: 919076]
18. Bershad N, Rockmore A. On estimating signal-to-noise ratio using the sample correlation coefficient. IEEE Trans. Inf. Theory 1974;20:112–113.
19. Frank J, Al-Ali L. Signal-to-noise ratio of electron micrographs obtained by cross correlation. Nature 1975;256:376–379. [PubMed: 1095934]
20. Wolter H. Spiegelsysteme streifenden Einfalls als abbildende Optiken für Röntgenstrahlen. Ann. Phys 1952;10:94–114. 286.
21. Henke BL, Gullikson EM, Davis JC. X-ray Interactions: Photoabsorption, Scattering, Transmission, and Reflection at E=50–30,000 eV, Z=1–92. Atomic Data and Nuclear Data Tables 1993;54:181–342.
22. London RA, Rosen MD, Trebes JE. Wavelength choice for soft x-ray laser holography of biological samples. Appl. Opt 1989;28:3397–3404. [PubMed: 20555712]
23. Cowley JM, Moodie AF. Fourier Images. I. The Point Source. Proceedings of the Physical Society B 1957;70:486–496.
24. Thibault P, Elser V, Jacobsen C, Shapiro D, Sayre D. Reconstruction of a yeast cell from x-ray diffraction data. Acta Crystallographica A 2006;62:248–261.
25. Schneider G, Anderson E, Vogt S, Knöchel C, Weiss D, Legros M, Larabell C. Computed tomography of cryogenic cells. Surf. Rev. Lett 2002;9:177–183.
26. Kirz J. Phase zone plates for X rays and the extreme UV. J. Opt. Soc. Am 1974;64:301–309.
27. Goodman, JW. Introduction to Fourier Optics. San Francisco: McGraw-Hill; 1968.
28. Elser V. Phase retrieval by iterated projections. J. Opt. Soc. Am. A 2003;20:40–55.
29. Howells M, Beetz T, Chapman H, Cui C, Holton J, Jacobsen C, Kirz J, Lima E, Marchesini S, Miao H, Sayre D, Shapiro D, Spence J, Starodub D. An assessment of the resolution limitation due to radiation-damage in x-ray diffraction microscopy. J. Electron. Spectrosc. Relat. Phenom 2009;170:4–12.
30. Shen Q, Bazarov I, Thibault P. Diffractive imaging of nonperiodic materials with future coherent x-ray sources. J. Synchrotron. Radiat 2004;11:432–438. [PubMed: 15310961]
31. Rose A. Unified approach to performance of photographic film, television pickup tubes, and human eye. J. Soc. Motion Pict. Eng 1946;47:273–294.
32. Shapiro D, Thibault P, Beetz T, Elser V, Howells M, Jacobsen C, Kirz J, Lima E, Miao H, Neiman AM, Sayre D. Biological imaging by soft x-ray diffraction microscopy. Proc. Natl. Acad. Sci. USA 2005;102:15343–15346. [PubMed: 16219701]
33. Chapman H, Barty A, Marchesini S, Noy A, Hau-Riege SP, Cui C, Howells M, Rosen R, He H, Spence J, Weierstall U, Beetz T, Jacobsen C, Shapiro D. High resolution *ab initio* three-dimensional x-ray diffraction microscopy. J. Opt. Soc. Am. A 2006;23:1179–1200.
34. Thibault P, Dierolf M, Menzel A, Bunk O, David C, Pfeiffer F. High-resolution scanning x-ray diffraction microscopy. Science 2008;321:379–382. [PubMed: 18635796]
35. Williams G, Quiney H, Peele A, Nugent K. Coherent diffractive imaging and partial coherence. Phys. Rev. B 2007;75(104):102.

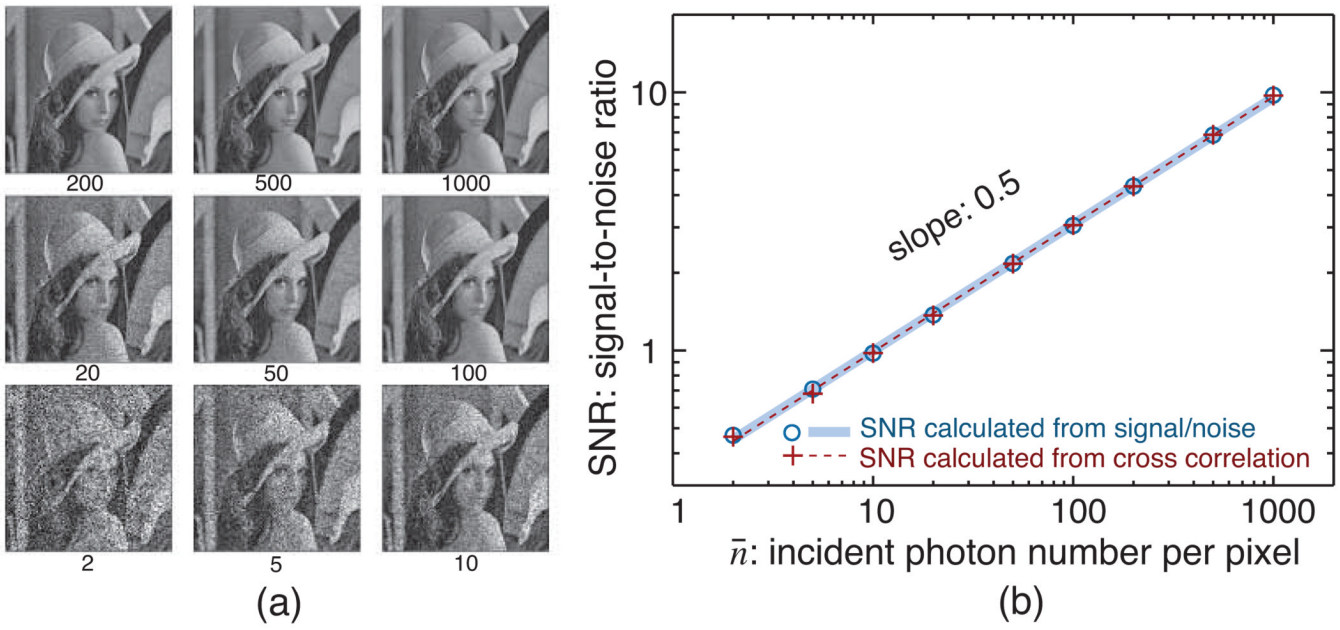

Fig. 1.

(a) Images with noise simulated according to different mean photon numbers per pixel n^-. Without noise, each pixel p has a value I_p of between 0 and 1. With illumination of n^- photons per pixel, each pixel has a starting value of $\bar{n}I_p$ photons which was used on a pixel-by-pixel basis to generate an image using signal-dependent noise calculated using the positive-integer-truncated Gaussian approximation. (b) signal-to-noise ratio (SNR) calculated from the images versus incident photon number per pixel n^-. The signal-to-noise ratio was calculated both by comparison of the noisy image with the noise-free original image described in Eqs. (7) and (8), and by using the two-noisy-image correlation method described in Eqs. (11) and (14). Since a fit of the data on a log-log plot of SNR versus n^- shows a slope of 0.5 as expected from Eq. (5), both image SNR methods give the expected scaling of SNR versus exposure n^-.

NIH-PA Author Manuscript
NIH-PA Author Manuscript
NIH-PA Author Manuscript

NIH-PA Author Manuscript

NIH-PA Author Manuscript

NIH-PA Author Manuscript

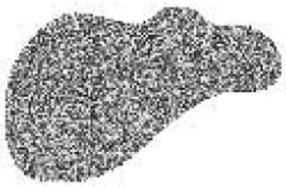

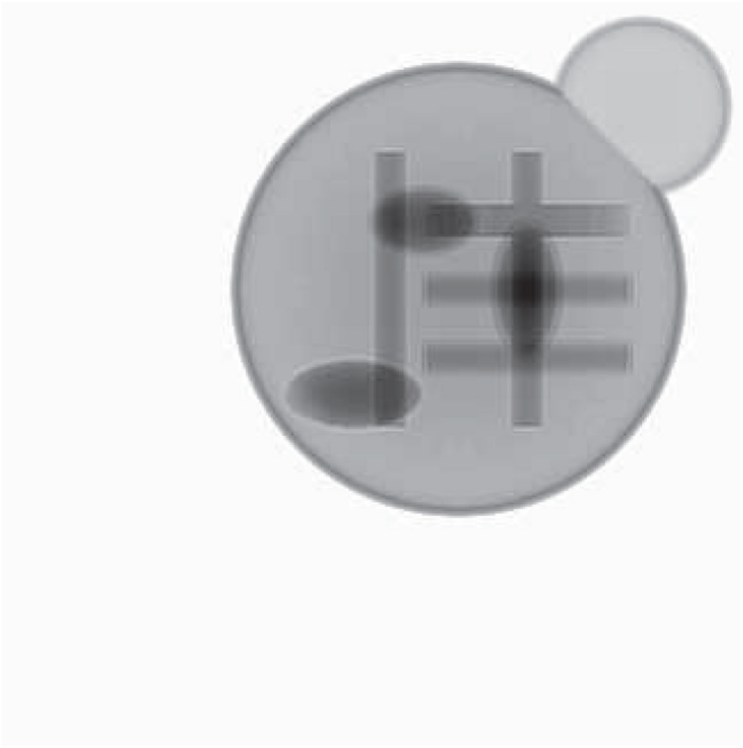

Cell A

Cell B

Fig. 2.

Defined objects used for image simulations. Shown here are the magnitudes of the simulated exit waves resulting from plane wave illumination of the objects. Cell A has random protein thicknesses within an irregular boundary, while Cell B has a lipid membrane and several protein bars and ellipses inside.

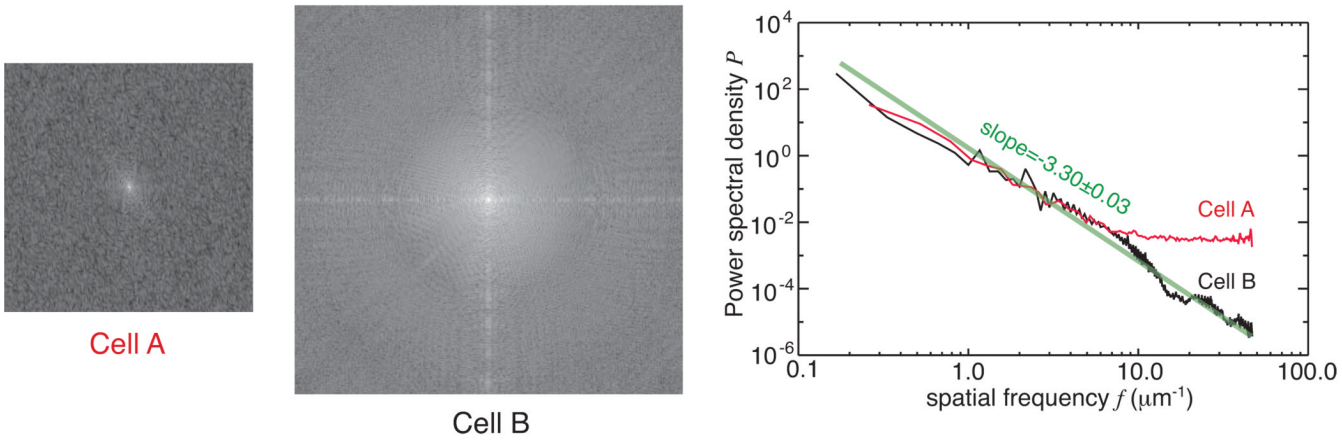

Fig. 3.

Diffraction patterns of the exit waves from the two defined objects, cell A and cell B, and their azimuthally averaged, unit-integral-normalized power spectral densities. In both cases the exit wave amplitudes were Fourier transformed and then squared to yield the diffraction intensity. Both defined objects have the signal decline with spatial frequency in a power law relationship with a slope of about 3.3 over most frequencies. For cell A, this trend then levels off at a spatial frequency of about 10 μm^{-1} where the pixel-by-pixel uncorrelated protein thickness dominate the diffraction pattern; this yields a flat power spectrum corresponding to a delta (δ) function in real space. For cell B, the overall round shape of the object gives rise to Airy rings in the diffraction pattern which show up at spatial frequencies above 10 μm^{-1}.

NIH-PA Author Manuscript
NIH-PA Author Manuscript
NIH-PA Author Manuscript

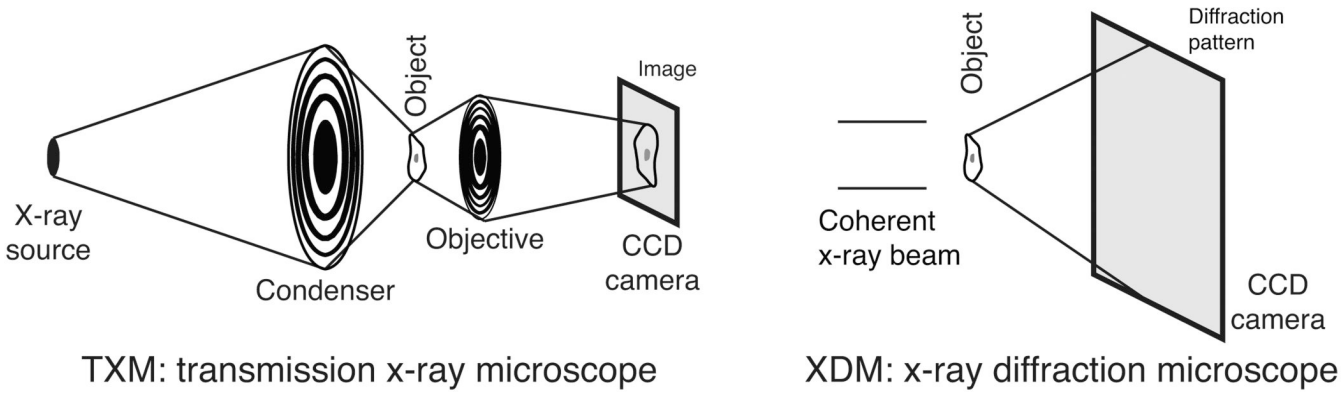

Fig. 4.

Schematic of the two x-ray imaging systems considered in simulations. In the TXM or transmission x-ray microscope at left, incoherent brightfield imaging is assumed where the numerical aperture of the condenser is 1.5 times the numerical aperture of the objective lens; a magnified image is recorded on a detector such as a CCD. The TXM objective is a zone plate with 30 nm outermost zone width and 10% diffraction efficiency. In XDM or x-ray diffraction microscopy at right, the specimen is assumed to be illuminated by a fully coherent beam and the far-field x-ray diffraction pattern is recorded on a detector such as a CCD. A reconstructed image is obtained by computational phasing of the coherent diffraction pattern.

NIH-PA Author Manuscript
NIH-PA Author Manuscript
NIH-PA Author Manuscript

NIH-PA Author Manuscript
NIH-PA Author Manuscript
NIH-PA Author Manuscript

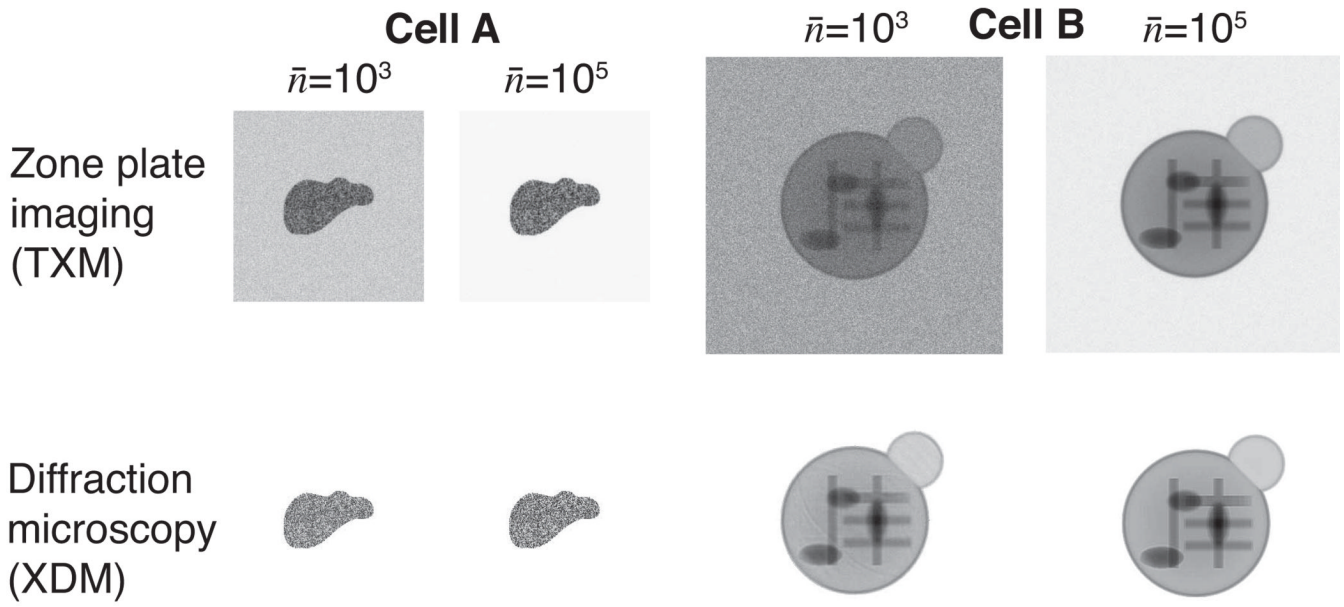

Fig. 5.

Images resulting from the simulations. Shown here are both TXM (top row) and XDM (bottom row) images calculated for the two defined objects, cells A and B, with exposures of $\bar{n} = 1 \times 10^3$ and $\bar{n} = 1 \times 10^5$ photons per pixel. The lack of "salt and pepper" shot noise in background region outside of the cell in the XDM reconstructions is a result of the imposition of a finite support constraint in the reconstruction process.

NIH-PA Author Manuscript
NIH-PA Author Manuscript
NIH-PA Author Manuscript

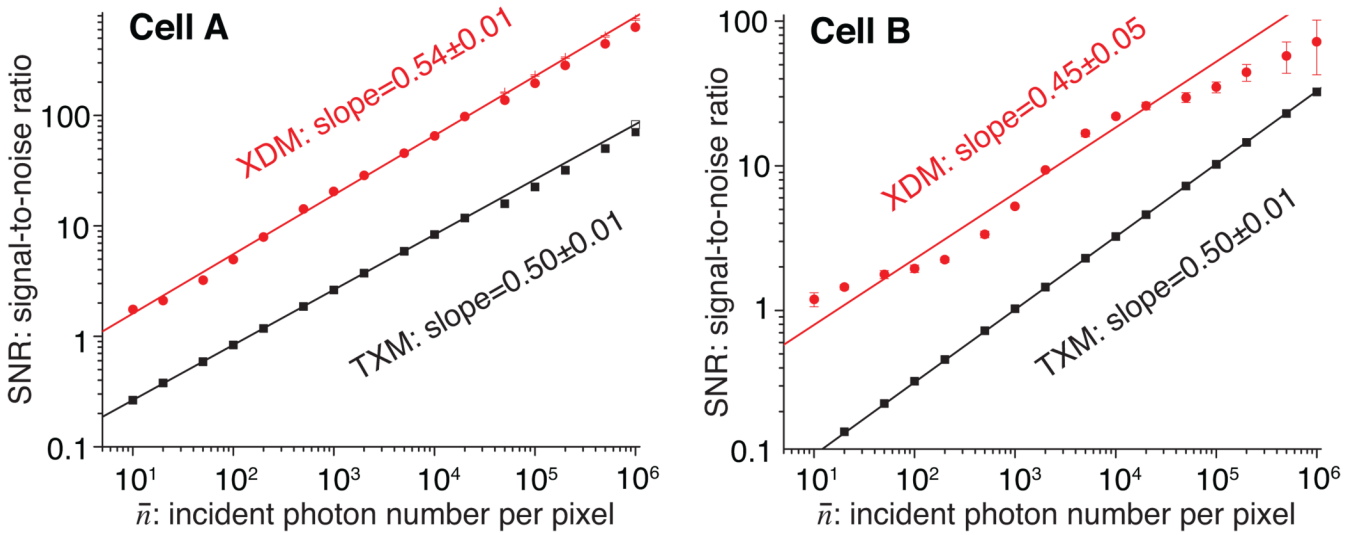

Fig. 6.

Plots of the signal-to-noise ratio SNR as a function of incident photons per pixel n^{-} for our simulation set. The results at left are for the defined object “cell A”, while those at right are for “cell B” (see Fig. 2). The results for both x-ray diffraction microscopy (XDM) and transmission x-ray microscopy (TXM) are shown. In each case a slope of about 1/2 is observed in the $\log_{10}(\text{SNR})$ versus $\log_{10}(n^{-})$ plot (Eq. (5)), and for both objects the SNR for x-ray diffraction microscopy is about 7 times higher than it is for transmission x-ray microscopy. For x-ray diffraction microscopy of cell B, the SNR curve oscillates around the straight line fit. This oscillation corresponds to providing enough signal to phase data in successive Airy rings in the diffraction pattern of the overall spherical shape of cell B, as shown in Fig. 3.

NIH-PA Author Manuscript
NIH-PA Author Manuscript
NIH-PA Author Manuscript

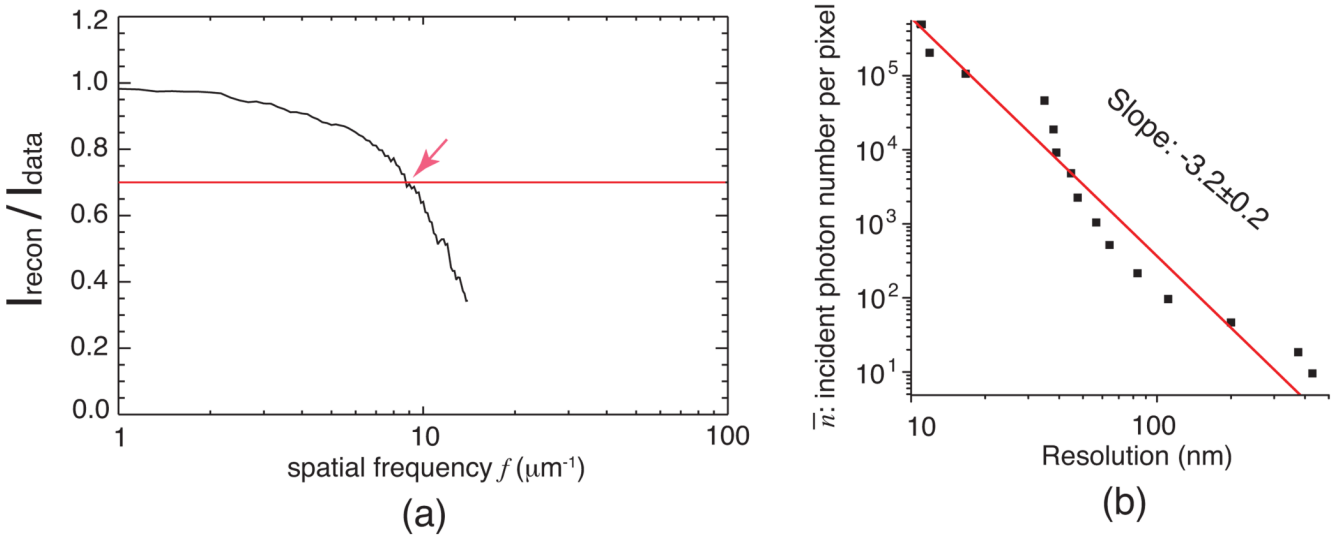

Fig. 7.

Investigation of the dose versus resolution trend for x-ray diffraction microscopy of defined object B. (a) The ratio $\langle I_{\text{recon}}(f)\rangle / \langle I_{\text{data}}(f)\rangle$ for the example case of incident photon number $\bar{n} = 1000$. This ratio measures how consistent the reconstructed intensity I_{recon} averaged over many iterates compared to the recorded intensity I_{data}. We chose a cutoff value of 0.7 as providing an estimate of the resolution of the reconstructed image. (b) The resulting trend of incident photon number $\bar{n}$ versus resolution Δ_{min}, along with a straight line fit to determine the dose versus resolution scaling parameter m_r. The value of $m_r = -3.2 \pm 0.2$ is consistent with the scaling of $m = -3.30 \pm 0.03$ shown in Fig. 3 for the diffracted signal from this object.